Title: HER3-Mediated Resistance to Hsp90 Inhibition Detected in Breast Cancer Xenografts by Affibody-based PET Imaging

Authors: Carlos D. Martins[1], Chiara Da Pieve[1], Thomas A. Burley[1], Rhodri Smith[1], Daniela M. Ciobota[1], Louis Allott[1], Kevin J. Harrington[1], Wim J.G. Oyen[1, 2], Graham Smith[1], Gabriela Kramer-Marek[1*]

Affiliations:

[1]Division of Radiotherapy and Imaging, The Institute of Cancer Research, 123 Old Brompton Road, London, SW7 3RP, UK

[2]The Royal Marsden NHS Foundation Trust, Department of Nuclear Medicine, Fulham Road, London, SW3 6JJ, UK

Running title:
HER3 PET Imaging as a Biomarker of Drug Resistance

Keywords:
HER3, affibody-based PET imaging, Hsp90 inhibition, breast cancer

Financial support: This research was supported in part by the by the Cancer Research UK-Cancer Imaging Centre (C1060/A16464) and EPSRC (EP/H046526/1).

Corresponding author:
*Gabriela Kramer-Marek
123 Old Brompton Road, London, SW7 3RP, UK
Phone: +44 208 722 4412
Email: Gabriela.Kramer-Marek@icr.ac.uk

Conflict of interest statement: The authors declare no potential conflicts of interest.

Word count (excluding references): 5018

Total number of figures and tables:

Figures: 6

Supplementary Figures: 18

Supplementary Tables: 8

Supplementary Movies: 2

Translational Relevance

Currently, inter- and intra-tumor heterogeneity is a clinical challenge, as histological techniques can fail to provide a representative indication of molecular variation, due to dependence on the section of tumor that is chosen for sampling. This underscores the need to introduce novel imaging biomarkers that allow the examination of the whole tumor mass and may significantly help to better understand and treat cancer. Therefore, we have developed a novel PET radiotracer that will provide information on heterogeneous HER3 expression and receptor expression changes due to downstream signaling inhibition, which is increasingly being recognized as a key player in therapeutic resistance. This would aid in the selection of patients for novel HER3 targeted therapies and potentially enable patients to be spared ineffective therapies, and, if necessary, being switched sooner to more effective therapeutic regimens.

Abstract

Purpose: Recent studies have highlighted a role of human epidermal growth factor receptor 3 (HER3) in HER2-driven cancers (e.g. breast cancer) implicating the up-regulation of the receptor in resistance to HER-targeted therapies and Hsp90 inhibitors (e.g. AUY922). Therefore, we have developed an affibody-based PET radioconjugate that quantitatively assesses HER3 changes induced by Hsp90 inhibition *in vivo*.

Experimental Design: $Z_{HER3:8698}$ affibody molecules were conjugated via the C-terminus cysteine to DFO-maleimide for ^{89}Zr radiolabeling. The probe was characterized *in vitro* and *in vivo* in a panel of human breast cell lines and xenograft models with varying HER3 receptor levels. Additionally, the radioconjugate was investigated as a tool to monitor the outcome of AUY922, an Hsp90 inhibitor in MCF-7 xenograft model.

Results: We demonstrated that ^{89}Zr-DFO-$Z_{HER3:8698}$ can track changes in receptor expression in HER3-positive xenograft models and monitor the outcome of AUY922 treatment. Our *in vitro* findings showed that MCF-7 cells, which are phenotypically different from BT474, develop resistance to AUY922 through HER3/IGF-1Rβ-mediated signaling. Of note, the lack of response *in vitro* due to HER3 recovery was confirmed *in vivo* using ^{89}Zr-DFO-$Z_{HER3:8698}$-based imaging. Upon AUY922 treatment, higher radioconjugate uptake was detected in treated MCF-7 xenografts, correlating with an AUY922-induced HER3 up-regulation concomitant with an increase in IGF-1Rβ expression.

Conclusion: These data underline the potential of HER3-based PET imaging to noninvasively provide information about HER3 expression and to identify patients not-responding to targeted therapies due to HER3 recovery.

Introduction

The epidermal growth factor receptor 3 (HER3), a member of the HER family of receptor tyrosine kinases, is a key driver of carcinogenesis (1, 2). Relative to other family members, HER3 has diminished kinase activity and its phosphorylation depends on dimerization with other receptors. The HER2-HER3 heterodimer is the most potent HER family dimer, but HER3 also dimerizes with EGFR (HER1) and cross-talks with other non-HER family members, such as c-Met and IGF-1Rβ. Recent studies have highlighted HER3 critical role in tumor progression and have defined its importance in the development of resistance to targeted therapies. In fact, EGFR- and HER2-driven cancers frequently become unresponsive to anti-HER targeted therapeutics and inhibitors of the downstream PI3K/AKT/mTOR pathway through compensatory activation of HER3-mediated signaling which bypasses the original therapeutic blockade (3). The same may be true for heat shock protein 90 (Hsp90) inhibitors (e.g. AUY922), which are known to interfere with the post-translational folding of several oncogenic client proteins (e.g. HER2, HER3 and AKT) and have shown moderate therapeutic efficacy in breast cancer (BC) (4-6). For example, a strong association between sensitivity to anti-HER2 inhibitors, including trastuzumab and lapatinib, and HER3 protein up-regulation has been demonstrated using both BC cell lines and core biopsies of HER2+ tumors from BC patients (7, 8). In addition, combining an AKT inhibitor with either lapatinib or PF-04929113 (Hsp90 inhibitor) prevented the feedback-mediated induction of phosphorylated HER3, highlighting the fact that targeted therapies against HER3 are synergistic with multiply PI3K inhibitors (9).

Given the importance of HER3 signaling, several monoclonal antibodies (mAbs) targeting the receptor ectodomain have recently been developed, with some already in phase I and II clinical trials (i.e. MM-121, patritumab, LJM716 and KTN3379) (10, 11). Investigations conducted with LJM716 highlighted significant growth inhibitory effects in HER2-positive cells and BC xenograft models when combined with trastuzumab (12, 13). Moreover, KTN3379 combined with trastuzumab yielded greater and more durable tumor regression in both ligand-dependent and -independent BC models with different levels of HER2 expression and sensitivity to HER2-targeted drugs (14). Despite promising results from clinical trials, the success of HER3-targeting therapies is likely to depend on the development of reliable HER3-specific biomarkers (15, 16). In this context, consideration has been given to natural ligands, which activate HER3 including NRG-1/HRG (17). However, even though NRG-1 is the most potent inducer of HER3 phosphorylation, it may be of limited utility as a biomarker given the fact that there are multiple routes of HER3 activation including mutations, ligand-independent dimerization and interactions with other HER and non-HER family ligands (2). Currently, the activation status of HER3 is analyzed by methods such as immunohistochemistry (IHC), proteomics and RNA-based technologies that rely on tissue obtained at biopsy or at surgical resection. These invasive procedures might not accurately address inter- and intra-tumor heterogeneity that may exist within the same tumor deposit or within different lesions in the same patient (18).

These considerations make a strong case for developing an imaging biomarker of drug response to therapies affecting HER3 expression allowing physicians to tailor treatment regimens to patient-specific biology. Recently, anti-HER3 mAbs, anti-HER3-F(ab')$_2$ were radiolabeled with ^{64}Cu and ^{89}Zr for molecular imaging of HER3 expression (19-22). ^{89}Zr radiolabeled mAb (GSK2849330) is currently being evaluated in patients with advanced solid tumors (NCT02345174). However, clinical use of full-length mAbs as imaging agents is not optimal, due to their long biological half-life and relatively slow tumor penetration, both of which affect tumor-to-background contrast at early time points (23). To circumvent these issues, we, and others, have recently developed low molecular weight (~7 kDa) affibody-based positron emission tomography (PET) imaging agents that recognize HER3 on the cellular membrane (24, 25).

Here, we demonstrate using breast adenocarcinoma cell lines that HER3 expression changes induced by Hsp90 inhibition *in vitro* can also be quantitatively measured following AUY922 treatment in BC xenograft models by ^{89}Zr-DFO-$Z_{HER3:8698}$ imaging. Texture analysis of PET images permitted a clear distinction between control and treated mice providing evidence for alternative and more robust image analysis than simple uptake metrics. In the future, clinical application of $Z_{HER3:8698}$-based radioconjugates can be of use to guide the treatment decisions for BC patients by providing specific information on therapy-induced HER3 receptor changes in a non-invasive manner.

Materials and Methods

Cell lines

Human breast adenocarcinoma (MCF-7, BT-474, MDA-MB-468 and MDA-MB-231) cell lines were obtained from the American Type Tissue Culture Collection (ATCC, USA). MCF-7-Tet-Off-HER2 cell line was kindly donated by Professor Joaquin Arribas and maintained as previously described (26). All cell

lines were tested and authenticated by short tandem repeat (STR) DNA profiling analysis. The cells were cultured in DMEM (MCF-7, MDA-MB-231), RPMI1640 (BT-474, MDA-MB-468) or DMEM/Ham/F12 (MCF-7-Tet-Off-HER2) with high glucose (Gibco, Life Technologies, UK) and supplemented with 10% fetal bovine serum (FBS), (Gibco, Life Technologies, UK). Additionally, DMEM/Ham/F12 contained 1 μg/mL of doxycycline (Sigma, UK), 0.2 mg/mL of neomycin (Sigma, UK), and 0.1 mg/mL of hygromycin (Life Technologies, UK). All cell lines were maintained at 37°C in a humidified atmosphere supplied with 5% CO_2.

Drug treatments

AUY922 and Picropodophyllin (PPP) were purchased from LC Laboratories (USA) and Stratech Scientific (UK), respectively. Both compounds were dissolved in 100% dimethyl sulfoxide (DMSO, Sigma-Aldrich, UK) and diluted with culture medium to a desired concentration, with a final DMSO concentration <0.1% (v/v). Unless otherwise stated, the cell lines were exposed to 32 nM of AUY922 and/or 10 μM of PPP for 48 h (27, 28).

Preparation of ^{89}Zr-labeled DFO-affibody conjugates

The conjugation of deferoxamine-maleimide (DFO-mal, Macrocyclics, USA) to the $Z_{HER3:8698}$-Cys and Z_{TAQ}-Cys affibody molecules (Affibody, Sweden), ^{89}Zr-radiolabeling procedures as well as the *in vitro* serum stability of ^{89}Zr-DFO-$Z_{HER3:8698}$ are described in detail in the Supporting Information.

^{89}Zr-DFO-$Z_{HER3:8698}$ *in vitro* binding affinity and specificity

The dissociation constant (K_d) and the specificity of binding of ^{89}Zr-DFO-$Z_{HER3:8698}$ were assessed as previously described (24). A detailed description of the procedure is given in the Supporting Information.

Animal studies

The detailed methods are described in the Supporting Information. Briefly, animal experiments were performed on 6-8 week-old female NCr athymic mice (Charles River, UK) or NSG (NOD-Scid Gamma, the Jackson Laboratory) in compliance with license issued under the UK Animals (Scientific Procedures) Act 1986 and approved by the institutional ethical review according to the United Kingdom National Cancer Research Institute Guidelines for Animal Welfare in Cancer Research (29). Mice were inoculated subcutaneously (s.c.) on the shoulder with MCF-7, BT-474, MDA-MB-468 or MDA-MB-231 cells (6.5×10^6) resuspended in PBS and mixed with BD Matrigel™ Matrix (7:3 v/v, BD Matrigel™ Matrix, BD Bioscience, UK).

PET imaging studies

PET/CT imaging studies were conducted using an Albira PET/SPECT/CT imaging system performed at 3 h post injection. (Bruker, UK). The detailed imaging and data analysis protocols are given in the Supporting Information.

***Ex vivo* biodistribution**

Mice were euthanized by cervical dislocation for biodistribution studies, 3 and 24 h post-tracer injection. The major organs/tissues were dissected, weighed, and their associated-radioactivity was measured in a gamma counter. The %ID/g was determined for each organ/tissue. Unless otherwise stated, the data were expressed as the mean of $n = 3$ mice ± SD.

During AUY922 treatment study, the overall tumor volumes in some mice were significantly reduced which limited the use of all xenografts for *ex vivo* biodistribution studies.

Immunohistochemistry

Formalin-fixed tumors (10%, v/v) were embedded in paraffin, sectioned into 3 μm-thick slices, and mounted on microscope slides. The detailed staining procedures with the various antibodies are described in the Supporting Information.

Tumor *ex vivo* autoradiography

Tumors were dissected and immediately embedded in an optimal-cutting-temperature compound (Tissue-Tek, USA), frozen on dry ice and subsequently processed as previously described (30). Further experimental details are given in the Supporting Information.

Immunoblotting analysis
Western blotting (WB) was carried out as previously described (31). A complete list of used antibodies and the detailed methods are provided in the Supporting Information.

Immunoprecipitation
Tissue lysates (300 μg) and whole cell lysates (200 μg) were incubated overnight in a thermomixer at 4°C and 650 rpm, with 10 μg of anti-HER3 mouse mAb (Merck Millipore, UK). Following formation of the antibody-antigen complex, the immunocomplexes were purified using Dynabeads ProteinA (Life Technologies, UK) according to the manufacturer's instructions. The immunoprecipitates were analyzed by WB.

Proliferation and scratch-wound assays
MCF-7 and BT-474 cells were used for proliferation and scratch-wound assays with an Incucyte Zoom imaging system (Essen BioScience, USA) according to the protocols provided by the manufacturer. Detailed descriptions of the procedures and image analysis are described in the Supporting Information.

Statistical analyses
Unless otherwise stated, data were expressed as the mean ± SD. Statistical significance, sample size calculations and correlation analysis are described in detail in the Supporting Information.

Results

Hsp90 inhibition promotes HER3/IGF-1Rβ signaling in BC cells with low HER2 expression

To identify HER3-mediated drug resistance, we focused on the role of Hsp90 inhibition on HER3 signaling using two BC cell lines with different HER2 levels, BT-474 (HER2+++, HER3+++) and MCF-7 cells (HER2+, HER3+++). Both cell lines were treated with AUY922 for up to 48 h and subsequently, the expression levels of HER receptors and PI3K/AKT pathway activity were assessed by WB. Increased Hsp70/72 expression was used as a marker of efficient Hsp90 inhibition (32). In BT-474 cells, Hsp90 inhibition induced a down-regulation of both total and phosphorylated HER2 and HER3 (pHER2-Y1248 and pHER3-Y1289, respectively) as early as 8 h after treatment, concomitantly with the loss of PI3K/AKT signaling, as shown by a decrease in phosphorylated (pAKT-S473) and total AKT (Fig. 1A). Furthermore, EGFR and phosphorylated EGFR (pEGFR-Y1068), IGF-1Rβ, and c-Met were down-regulated 48 h following AUY922 treatment (Supplementary Fig. S1). Densitometric analysis of 2 independent experiments revealed a decrease 48 h after AUY922 treatment in the expression of both HER3 and IGF-1Rβ , of 0.38 ± 0.12 and 0.62 ± 0.01, respectively. Similarly, in MCF-7 cells, which have low HER2 expression, Hsp90 inhibition caused a down-regulation of c-Met. The total and phosphorylated HER2 and EGFR levels were undetectable and only a transient down-regulation of HER3/pHER3-Y1289 was found, followed by a HER3 recovery and activation 48 h after treatment initiation. Additionally, increased PI3K and pAKT-S473 levels at 48 h post-treatment indicated HER3-mediated activation of this pathway (Fig. 1A). Furthermore, HER3 and IGF-1Rβ expression levels in response to Hsp90 inhibition were determined by densitometry to be 0.99 ± 0.19 and 1.20 ± 0.52, respectively. The prevalence of IGF-1Rβ levels suggested this receptor as the potential HER3 dimerization partner in MCF-7 cells following AUY922-mediated HER2 down-regulation. To study this process, BT-474 and MCF-7 cells were treated with AUY922 alone or in combination with the IGF-1Rβ inhibitor PPP for 48 h with the expectation of reversing the HER3-mediated resistance. As shown in Fig. 1B and Fig S2, down-regulation of HER3, HER2, AKT, MAPK, IGF-1Rβ and c-Met was observed when BT-474 cells were treated with AUY922 alone or in combination with PPP. IGF-1Rβ inhibition alone was not effective in abrogating PI3K/AKT signaling, confirming the greater dependency of BT-474 cells on HER2-HER3 dimerization. Conversely, in MCF-7 cells, total and phosphorylated HER3 were not down-regulated to the same extent in response to Hsp90 inhibition, maintaining residual levels of phosphorylated AKT and MAPK. Importantly, in the presence or absence of HRG stimulation, HER3 levels were the same (Fig. 1B and Supplementary Fig. S3). However, inhibition of IGF-1Rβ reversed this phenotype suggesting a direct interaction between both receptors and the role of IGF-1Rβ in HER3-mediated signaling in response to Hsp90 blockade. Densitometric analysis of HER3 and IGF-1Rβ expression per treatment and per cell line is presented in Supplementary Table S1. To further verify the role of HER2 expression in inducing a HER3-mediated unresponsiveness to AUY922 treatment, MCF-7 cells overexpressing HER2 under the control of tetracycline (Tet-Off) were exposed to AUY922 and PPP for 48 h. HER2 was induced by the removal of doxycycline from the culture medium (MCF-7-HER2, -dox), (Fig. 1B). The effect of both inhibitors in MCF-7-HER2 (-dox, HER2+++) was similar

to that observed in BT-474 cells. Moreover, MCF-7-HER2 (+dox, HER2+) responded similarly to the parental MCF-7 (HER2+) cell line (Fig. 1B and Supplementary Fig. S2), confirming that high HER2 expression is required for efficient HER3 down-regulation in response to Hsp90 inhibition.

Given the role of HER3 in inducing PI3K/AKT signaling, the proliferative and invasive potential was assessed in response to AUY922 treatment and IGF-1Rβ inhibition. In BT-474 cells, proliferation was impaired in response to both treatment regimens, with a normalized confluence at 72 h post-treatment estimated to be 24-40% of that exhibited by the control cells (Fig. 1C and Supplementary Fig. S4A). On the other hand, AUY922 treatment alone did not affect the confluence of MCF-7 cells (Fig. 1D). The proliferative potential of these cells was counteracted by IGF-1Rβ inhibition, leading to normalized confluences of 22% (PPP alone) and 28% (AUY922 + PPP) at 72 h post-treatment (Fig. 1D and Supplementary Fig. S4A). Additionally, both Hsp90 and IGF-1Rβ inhibition showed an impact on wound invasion rates in BT-474 cells, with the relative wound densities (RWD) determined to be 19% (AUY922), 16% (PPP), and 15% (AUY922 + PPP), compared to 25% in control cells (Fig. 1E and Fig. S4B). However, in MCF-7 cells, Hsp90 inhibition resulted in a faster wound healing rate compared to control cells (95% and 85% RWDs, respectively) at 48 h. IGF-1Rβ blocking reduced the native and AUY922-induced invasive potential with RWDs of ~30% in both PPP alone and AUY922 combined with PPP, at 72 h post treatment (Fig. 1F and Supplementary Fig. S4B). These results highlight a greater impact of IGF-1Rβ inhibition on reducing the invasiveness of both cell lines. Importantly, these data were in agreement with the increased levels of N-cadherin observed in MCF-7 and MCF-7-HER2 (+dox) in response to AUY922 (Supplementary Fig. S2), suggesting a maintenance of the same level of invasiveness following Hsp90 inhibition.

^{89}Zr-DFO-$Z_{HER3:8698}$ uptake correlates with HER3 expression in breast adenocarcinoma cells

With the aim of monitoring changes in HER3 expression levels *in vivo* HER3 specific $Z_{HER3:8698}$ and non-specific Z_{TAQ} affibody molecules were radiolabeled with the long-lived positron emitter ^{89}Zr ($t_{1/2}$ = 78.4 h) as it enabled investigation of the pharmacokinetics (PK) of the conjugate at different time points. Of note, the $Z_{HER3:8698}$ molecules cross-react with HER3 of mouse origin making the PK studies more representative of the clinical setting. The DFO-affibody conjugates were characterized by high-performance liquid chromatography (HPLC) and mass spectrometry (Supplementary Fig. S5 and S6). The radiolabeling reaction of the conjugates with ^{89}Zr resulted in a >95% radiometal incorporation, as determined by instant thin layer chromatography (ITLC; Supplementary Fig. S7), and a specific activity of 2.5 - 2.7 MBq/μg (0.067 - 0.073 mCi/μg). The schematic structure of the ^{89}Zr-DFO-$Z_{HER3:8698}$ is shown in Fig. 2A. Stability studies showed that less than 3% de-metalation occurred after incubating ^{89}Zr-DFO-$Z_{HER3:8698}$ in mouse serum at 37°C for 3 h. The degree of de-metalation increased to ~15% after 24 h incubation (Supplementary Fig. S7 and S8). Receptor saturation binding analysis revealed the saturable binding of the radioconjugate to HER3 highly-expressing MCF-7 cells, with a mean dissociation constant (K_d) of 0.55 ± 0.05 nM and receptor density (B_{max}) of 21,896 ± 764 sites/cell (Fig. 2B). The specificity of ^{89}Zr-DFO-$Z_{HER3:8698}$ binding was assessed in a panel of BC cells, with MDA-MB-231 and BT-474 cells having the lowest and the highest HER3 expression levels, respectively (Fig. 2C and D). Pre-incubating the cells with either 100-fold molar excess of non-radiolabeled $Z_{HER3:8698}$ or HRG (competing for the same binding site), significantly reduced ^{89}Zr-DFO-$Z_{HER3:8698}$ binding (Fig. 2D). Importantly, the measured cell-associated radioactivity was in agreement with the HER3 protein levels per cell line (Fig. 2C and D).

^{89}Zr-DFO-$Z_{HER3:8698}$ accumulates in HER3-expressing BC xenografts

The specific uptake of ^{89}Zr-DFO-$Z_{HER3:8698}$ (3 μg of protein; 7.2-8.1 MBq/mouse) was evaluated 3 h post-radioconjugate administration using mice bearing subcutaneous BC xenografts with different HER3 expression levels. The obtained static PET/CT images allowed an accurate delineation of volumes of interest (VOI) in the case of both MCF-7 and MDA-MB-468 xenografts compared to MDA-MB-231 (Fig. 3A). Additionally, MCF-7 xenografts imaged with ^{89}Zr-DFO-Z_{TAQ}, exhibited negligible tumor uptake, further confirming the *in vivo* specificity of ^{89}Zr-DFO-$Z_{HER3:8698}$ (Fig. 3A). The PET imaging data were corroborated by *ex vivo* biodistribution studies (Fig. 3B, Supplementary Fig. S9, and Supplementary Table S2), with MCF-7 xenografts showing a tumor uptake of 2.67 ± 0.32 percent of the injected dose per gram of tissue (%ID/g ± SD), with tumor-to-blood and tumor-to-muscle ratios of 4.75 and 20.4, respectively. Conversely, lower tumor uptakes were measured in MDA-MB-468 (1.28 ± 0.13 %ID/g) and MDA-MB-231 (0.55 ± 0.25 %ID/g) xenograft models (Fig. 3B and Supplementary Table S2). As anticipated, low tumor uptake was also observed in MCF-7 xenografts injected with ^{89}Zr-DFO-Z_{TAQ} (0.17 ± 0.04 %ID/g) (Fig. 3A, B). Amongst the non-target expressing organs, the kidneys exhibited the highest accumulation of ^{89}Zr-DFO-$Z_{HER3:8698}$ with the uptake ranging from ~80 to 165 %ID/g across different

xenografts. This uptake occurs due to the glomerular filtration of the affibody molecules followed by radioconjugate reabsorption, degradation and retention in proximal tubular cells (33). Additionally, ^{89}Zr-DFO-$Z_{HER3:8698}$ was detected in other HER3-expressing normal organs such as lungs, liver and intestines (25).

The biodistribution data collected 24 h post-injection of ^{89}Zr-DFO-$Z_{HER3:8698}$ showed a decrease in the MCF-7 tumor signal which may be due to the release of the radionuclide from the conjugate *in vivo* (the stability measured in the serum was approximately 84% at 24 h). Consequently, as free zirconium-89 is known to accumulate in the mineral components of the bone, an increase in bone uptake was detected (34). The tumor-to-organ ratios were lower for the majority of the non-target tissues in comparison to the results obtained at 3 h (Supplementary Tables S3 and S4).

The tumor targeting by the radioactive agent observed in the various models, correlated with the HER3 expression per xenograft assessed by WB analysis of HER receptors, and HER3 IHC staining (Fig. 3C and D). Furthermore, autoradiography of tumor tissue slices highlighted a difference in radioactivity accumulation in MCF-7 tumors when compared to MDA-MB-468 and MDA-MB-231 (Fig. 3E). Three-dimensional (3D) segmentation of the tumor volumes further highlighted heterogeneous uptake, particularly in MCF-7 xenografts (Fig. 3F; the corresponding 3D movie is displayed as Supplementary Movie S1).

^{89}Zr-DFO-$Z_{HER3:8698}$ imaging can identify HER3-mediated resistance to Hsp90 inhibition in BC xenografts

In light of the effects of AUY922 treatment on HER3 expression observed *in vitro* (Fig. 1 and Supplementary Fig. S1-4), it was hypothesized that ^{89}Zr-DFO-$Z_{HER3:8698}$ could monitor HER3 recovery in response to Hsp90 inhibition *in vivo*. A pilot study was designed to test this hypothesis using MCF-7 and BT-474 xenografts. At the end of the AUY922 treatment the image-derived radioactivity concentration (%ID/g normalized to the initial values obtained on day 0) for MCF-7 tumor bearing mice (Fig. 4A; the corresponding 3D movie is displayed as Supplementary Movie S2) showed a statistically significant difference between control and treated groups (P = 0.0131), with the treatment group displaying a ~54% greater %ID/g ratio (1.23 ± 0.33) than the control group (0.80 ± 0.06; Fig. 4B).

These results were in agreement with the e*x vivo* measurements, which showed a more prominent tumor targeting of the radioconjugate in the treatment group (1.56 ± 0.10 %ID/g) compared to the control animals (1.15 ± 0.14 %ID/g) with a P = 0.0036 (Fig. 4C and Supplementary Fig. S10). The more intense HER3 staining of tumor sections in the treated xenografts further confirmed that greater %ID/g ratios were due to HER3 restoration following Hsp90 inhibition (Fig. 4D). Moreover, CD31 staining showed no discernible difference in vessel density between control and treated mice, indicating the observed effects were unlikely to relate to AUY922-induced alterations of the vasculature (Fig. 4D and Supplementary Fig. S11), as previously reported in BT-474 xenografts (27). Furthermore, no significant differences were observed in terms of tumor volume between control and treated mice (Supplementary Fig. S12). Importantly, the same treatment using BT-474 xenografts resulted in a significantly lower (P = 0.0009) ^{89}Zr-DFO-$Z_{HER3:8698}$ uptake in the treated mice (Supplementary Fig. S13).

^{89}Zr-DFO-$Z_{HER3:8698}$ texture analysis identifies AUY922-treated xenografts and correlates with *ex vivo* treatment response

Recently, several studies have demonstrated that texture analysis in cancer imaging provides a high throughput extraction of quantitative imaging biomarkers and assists in the design of descriptive and predictive models of tumor phenotypes (35, 36). We postulated that multiple texture features extracted from ^{89}Zr-DFO-$Z_{HER3:8698}$ images would provide a more comprehensive analysis of AUY922 treatment response, rather than a single, gross measure such as $[\%ID/g]_{max}$ or $[\%ID/g]_{mean}$ (Supplementary Fig. S9). Additionally, a predictive classification model to distinguish between control and treated mice was built using Linear Discriminant Analysis (LDA), a method that aims to minimize intra-class and maximize inter-class scatter, thus providing a linear combination of features that characterizes or separates the two classes, i.e. control and treated. The study workflow is described in Fig. 5A. A total of 89 parameters were extracted, out of which, 63 were more evidently different between control and treated groups. The ratios of post-/pre-treatment texture parameters are depicted in Fig. 5B and Supplementary Fig. S14A, presenting a distinction between control and treated xenografts. Moreover, the LDA models were assessed by examining their ability in successfully classifying the test mouse, as treated or control. For instance, assigning control mouse 1 (C_1) as the test subject in the %ID/g-based LDA model, resulted in a borderline separation between control and treated mice (Fig. 5C). Interestingly, using the texture-based LDA model with the same test subject (C_1) provided a more accurate and robust separation between the

two classes (Fig. 5D). Of note, our analysis was unbiased given that all extracted texture parameters were included in the model design, circumventing the main issue related to false discovery rates in texture analysis reported by Chalkidou et al. (37).

Densitometric analysis of WB data (Fig. 6A) denoted a significantly greater expression of Hsp70/72 ($P < 0.0001$) in the treated xenografts, clearly confirming efficient Hsp90 inhibition. As expected, HER2 expression was low in both groups. Significant up-regulation of both HER3 ($P = 0.031$) and IGF-1Rβ ($P = 0.002$) were detected (Fig. 6A and B). Furthermore, no discernible differences in terms of phosphorylated or total AKT were observed between control and treated mice (Fig. 6A and B). HER3 expression variability assessed by Western blot is relatively high, most likely due to the fact this technique yields semi-quantitative data limited to a snapshot of the tumor microenvironment that is sampled (Supplementary Fig. S15). Thus, it does not represent the heterogeneous nature of the receptor expression in the entire tumor mass (Supplementary Fig. S16). Therefore, even though no obvious correlation was detected between the %ID/g ratios and HER3 expression as determined by Western blot (Supplementary Fig. S15). Such findings suggest a role for molecular imaging probes (e.g. radiolabeled HER3 specific affibody molecules) as surrogate metrics to monitor the spatial distribution of heterogeneous receptor expression. Strong correlations were observed between HER3 and Hsp70/72 protein levels (Pearson $r = 0.61$; $P = 0.0265$) (Fig. 6C), as well as between IGF-1Rβ and Hsp70/72 (Pearson $r = 0.73$; $P = 0.0049$) (Fig. 6D), confirming the induction of HER3-IGF-1Rβ signaling in response to AUY922 treatment. Additionally, the strong correlation between %ID/g ratios and Hsp70/72 protein levels (Pearson $r = 0.81$; $P = 0.0008$) confirmed the capacity to assess Hsp90 inhibition efficiency via ^{89}Zr-DFO-$Z_{HER3:8698}$ imaging (Fig. 6E). Various texture parameters were in agreement with HER3, IGF-1Rβ, and Hsp70/72 expression, with 41.6%, 58.4% and 77.5% of the parameters having a correlation of $\geq$ 0.35, respectively (Supplementary Fig. S14B).

Conversely to MCF-7, in BT-474 xenografts AUY922 treatment led to a decrease in HER2, HER3 and IGF-1Rβ (Supplementary Fig. S13C).

HER3 immunoprecipitation studies with MCF-7 and BT-474 cells, revealed a direct interaction between IGF-1Rβ and HER3 following AUY922 treatment in MCF-7 but not in BT-474 cells (Fig. 6F, Supplementary Fig. S17 and S18), highlighting a potential role for HER3-IGF-1Rβ complexes in the therapeutic efficacy of AUY922. The same interaction was observed following HER3 immunoprecipitation using MCF-7 control and AUY922-treated tumor tissues (Fig. 6F), thus supporting the formation of HER3-IGF-1Rβ dimers in response to Hsp90 inhibition in xenograft models with low HER2 background (Fig. 6F and Supplementary Fig. S17 and S18).

Discussion

Aberrant regulation of HER receptor tyrosine kinases (RTKs) is common in BC and, even though the introduction of molecularly targeted drugs has reduced relapses among BC patients (38, 39), acquired or *de novo* resistance is still observed in advanced and adjuvant disease settings (40). Several mechanisms have been reported and linked to anti-HER-mediated drug resistance including the up-regulation of HER3 receptors via a negative feedback loop with downstream PI3K/AKT/mTOR (41). Early identification of patients likely to resist to therapy could be facilitated by the development of imaging biomarkers capable of stratifying patients based on their individual HER3 expression changes in response to anti-HER inhibitors could have enormous implications on clinical practice.

Currently, ^{18}F-FDG is the most widely used radiopharmaceutical for PET, which has also shown utility to monitor response to different treatment regimens (42). However, ^{18}F-FDG accumulates in tissues with increased glucose consumption regardless of the specific molecular signature of the tumor (43). Therefore, it has limited use when selecting patient for targeted drugs where prior knowledge of a given receptor status is essential for treatment initiation. Given such limitations, HER3-specific mAbs, affibody molecules, nanobody constructs and peptides have been radiolabeled to visualize different levels of HER3 *in vivo* (21, 44-46). The studies presented herein further strengthen a contribution of PET-based molecular imaging to non-invasively assess increased abundance of HER3 in response to therapeutic intervention. To test our hypothesis, a novel affibody-based PET radioconjugate (^{89}Zr-DFO-$Z_{HER3:8698}$) which specifically binds to the extracellular domain of HER3 was developed and investigated in BC xenografts. From a clinical standpoint (e.g. radionuclide characteristics and availability) labelling with fluorine-18 would be more suitable for patient administration due to a lower radiation exposure burden and radioactive half-life ($t_{1/2}$ = 108 min) compatibility with the pharmacokinetics of the affibody molecules. Therefore in the meantime, we have also developed a F-18 labelled analogue of the ^{89}Zr-DFO-$Z_{HER3:8698}$ that is a promising avenue for future investigations (24).

We tested the Hsp90 inhibitor, AUY922 known to induce proteosomal degradation of HER2:HER3 heterodimers (4-6, 47, 48) *in vitro* using HER3-expressing cells (BT-474 and MCF-7). Interestingly, MCF-7 cells developed HER3-mediated resistance to AUY922 and the unresponsiveness to the inhibitor was correlated with HER2 baseline expression given the greater therapeutic efficacy in BT-474 cells. Furthermore, in MCF-7 cells 48 h post-AUY922 treatment, the drug triggered an alternative survival pathway promoting HER3/IGF-1Rβ heterodimerization and the lack of response to AUY922 was reversed by IGF-1Rβ suppression. Notably, the prominent activation of HER3/IGF-1Rβ complexes enhanced the invasive potential of MCF-7 cells without affecting cellular proliferation.

These *in vitro* findings demonstrating that residual HER3 levels may attenuate the anti-proliferative effects of AUY922 in cells with low HER2 expression led us to investigate whether ^{89}Zr-DFO-$Z_{HER3:8698}$ imaging could monitor the lack of response to Hsp90 inhibition *in vivo*. As expected, accumulation of the conjugate *in vivo* correlated with HER3 receptor levels present in different xenograft models that was also in line with recently published data (25). Furthermore, several groups, including ours, have previously shown that HER2-specific imaging agents labelled with a wide range of radionuclides can measure the effects of administrating Hsp90 inhibitors on HER2 down-regulation (31, 49, 50).

Herein, we report an important observation that following AUY922 treatment, a clear distinction in ^{89}Zr-DFO-$Z_{HER3:8698}$ accumulation between control and AUY922-treated mice is due to HER3 down- and up-regulation in BT-474 and MCF-7 xenografts, respectively.

These results were corroborated by texture analysis, whereby the applied algorithm resulted in a better separability between these two groups than the conventionally used PET quantification %ID/g-based treatment response values (corresponding to the standardized uptake value (SUV) in clinical studies). These data highlight the potential of using basic texture features extracted from PET images to establish links between spatial variability in a given tumor's architecture and mapping them with tumor-specific pathway activation profiles. The authors recognize that additional investigations are required in order to better understand the association between these different texture features and tumor and/or gene/protein expression, but such an approach clearly has the potential to assist in future clinical decision-making.

Additionally, the higher radioconjugate uptake detected in the treated xenografts correlated with Hsp90-induced up-regulation of HER3 expression. The evident increase in IGF-1Rβ levels in response to AUY922 treatment, together with immunoprecipitation studies, further confirmed a role for HER3-IGF-1Rβ heterodimerization in acquired resistance to Hsp90 inhibition. These effects observed in MCF-7 xenografts highlight the potential AUY922 resistance mechanism that could be associated to low HER2 and high HER3 expression.

Interestingly, Whitesell *et al.* have recently reported that MCF-7 cells treated with Ganetespib (Hsp90 inhibitor) proliferate to a greater extent and shRNA knockdown of Hsp90 leads to upregulation of IGF-1Rβ. Furthermore, MCF-7 xenografts treated with this inhibitor showed no statistically significant difference compared to control mice in terms of tumor growth and event-free survival (51). Together, these data are in agreement with the lack of effect of Hsp90 inhibition in MCF-7 cells and xenografts reported herein, and with a prominent role for IGF-1Rβ in HER3 signaling.

These results are also in agreement with gene expression analysis of the TCGA Provisional dataset with the largest number of breast invasive carcinoma samples (n = 1105), whereby a statistically significant co-occurrence of the expression of *HER3* and *IGF-1R* genes was found ($P = 0.020$, Table S5) (52). Moreover, alterations in these genes also correlated with shorter overall and disease-free survival rates (Tables S6 and S7). In contrast, using the same dataset, no statistically significant co-occurrence of *HER3* and *IGF-1R* genes was found in samples with up-regulated *HER2* expression (Table S8), further supporting a dependency on HER3-IGF-1Rβ-mediated signaling in the presence of low HER2 expression. Further work will be carried out in multiple BC xenograft models, to study the potential of HER3 and IGF-1Rβ therapeutics in overcoming the discussed resistance mechanism in response to Hsp90 inhibition and anti-HER2 targeted therapies.

In conclusion, consistent with the findings reported herein, several recent Hsp90 inhibitor-based clinical trials have shown that the use of such agents might not be an effective therapeutic strategy in BC (7-9, 44, 45). Therefore, studies comprising combinatorial therapeutic approaches with agents targeting enriched resistance-conferring receptors (e.g. HER3, IGF-1Rβ) may be required for a more effective clinical use of Hsp90 inhibitors. We believe that HER3 PET imaging may prove to be an important measure in quantifying changes in HER3 expression resulting from acquired resistance to Hsp90 inhibition and thus serve as a valuable tool in facilitating treatment personalization.

Acknowledgments

The authors gratefully thank AffibodyAB for supplying the affibody molecules. We thankfully acknowledge Professor Joaquin Arribas for donating the MCF-7-Tet-Off-HER2 cell line. We owe special thanks to Dr Terry Spinks for continuous help with PET/SPECT/CT imaging system. We thank Frances Daley and the Pathology Core Facility for immunohistochemistry assistance. We also appreciate the constructive comments from Prof. Martin Leach. In addition, the EPSRC UK National Mass Spectrometry Facility at Swansea University is thanked for provision of technical services.

Authors' Contribution

Conception and design: Carlos D. Martins, Gabriela Kramer-Marek

Development of methodology: Carlos D. Martins, Chiara Da Pieve, Graham Smith, Rhodri Smith, Gabriela Kramer-Marek

Acquisition of data (provided animals, acquired and managed patients, provided facilities, etc.): Carlos D. Martins, Daniela M. Ciobota, Thomas A Burley, Louis Allott

Analysis and interpretation of data (e.g., statistical analysis, biostatistics, computational analysis): Carlos D. Martins, Kevin J. Harrington, Gabriela Kramer-Marek

Writing, review, and/or revision of the manuscript: Carlos D. Martins, Chiara Da Pieve, Kevin J. Harrington, Thomas A Burley, Rhodri Smith, Wim J.G. Oyen, Graham Smith, Gabriela Kramer-Marek

Study supervision: Gabriela Kramer-Marek

References

1. Baselga J, Swain SM. Novel anticancer targets: revisiting ERBB2 and discovering ERBB3. Nature Reviews: Cancer. 2009;9:463-75.
2. Gala K, Chandarlapaty S. Molecular pathways: HER3 targeted therapy. Clinical Cancer Research. 2014;20:1410-6.
3. Amin DN, Campbell MR, Moasser MM. The role of HER3, the unpretentious member of the HER family, in cancer biology and cancer therapeutics. Seminars in Cell & Developmental Biology. 2010;21:944-50.
4. Kamal A, Thao L, Sensintaffar J, Zhang L, Boehm MF, Fritz LC, et al. A high-affinity conformation of Hsp90 confers tumour selectivity on Hsp90 inhibitors. Nature. 2003;425:407-10.
5. Wainberg ZA, Anghel A, Rogers AM, Desai AJ, Kalous O, Conklin D, et al. Inhibition of HSP90 with AUY922 induces synergy in HER2-amplified trastuzumab-resistant breast and gastric cancer. Molecular Cancer Therapeutics. 2013;12:509-19.
6. Safavi S, Jarnum S, Vannas C, Udhane S, Jonasson E, Tomic TT, et al. HSP90 inhibition blocks ERBB3 and RET phosphorylation in myxoid/round cell liposarcoma and causes massive cell death in vitro and in vivo. Oncotarget. 2016;7:433-45.
7. Garrett JT, Olivares MG, Rinehart C, Granja-Ingram ND, Sanchez V, Chakrabarty A, et al. Transcriptional and posttranslational up-regulation of HER3 (ErbB3) compensates for inhibition of the HER2 tyrosine kinase. P Natl Acad Sci USA. 2011;108:5021-6.
8. Narayan M, Wilken JA, Harris LN, Baron AT, Kimbler KD, Maihle NJ. Trastuzumab-induced HER Reprogramming in "Resistant" Breast Carcinoma Cells. Cancer Res. 2009;69:2191-4.
9. Chandarlapaty S, Sawai A, Scaltriti M, Rodrik-Outmezguine V, Grbovic-Huezo O, Serra V, et al. AKT inhibition relieves feedback suppression of receptor tyrosine kinase expression and activity. Cancer Cell. 2011;19:58-71.
10. Aurisicchio L, Marra E, Roscilli G, Mancini R, Ciliberto G. The promise of anti-ErbB3 monoclonals as new cancer therapeutics. Oncotarget. 2012;3:744-58.
11. Garner AP, Bialucha CU, Sprague ER, Garrett JT, Sheng Q, Li S, et al. An antibody that locks HER3 in the inactive conformation inhibits tumor growth driven by HER2 or neuregulin. Cancer Res. 2013;73:6024-35.
12. Garrett JT, Sutton CR, Kurupi R, Bialucha CU, Ettenberg SA, Collins SD, et al. Combination of antibody that inhibits ligand-independent HER3 dimerization and a p110alpha inhibitor potently blocks PI3K signaling and growth of HER2+ breast cancers. Cancer Res. 2013;73:6013-23.
13. Garner A, Sheng Q, Bialucha U, Chen DS, Chen Y, Das R, et al. LJM716: an anti-HER3 antibody that inhibits both HER2 and NRG driven tumor growth by trapping HER3 in the inactive conformation. Cancer Res. 2012;72.
14. Xiao Z, Carrasco RA, Schifferli K, Kinneer K, Tammali R, Chen H, et al. A Potent HER3 Monoclonal Antibody That Blocks Both Ligand-Dependent and -Independent Activities: Differential Impacts of PTEN Status on Tumor Response. Molecular Cancer Therapeutics. 2016;15:689-701.
15. Dey N, Williams C, Leyland-Jones B, De P. A critical role for HER3 in HER2-amplified and non-amplified breast cancers: function of a kinase-dead RTK. American journal of translational research. 2015;7:733-50.
16. Kol A, Terwisscha van Scheltinga AG, Timmer-Bosscha H, Lamberts LE, Bensch F, de Vries EG, et al. HER3, serious partner in crime: therapeutic approaches and potential biomarkers for effect of HER3-targeting. Pharmacology & therapeutics. 2014;143:1-11.
17. Schoeberl B, Faber AC, Li D, Liang MC, Crosby K, Onsum M, et al. An ErbB3 antibody, MM-121, is active in cancers with ligand-dependent activation. Cancer Res. 2010;70:2485-94.
18. Kurozumi S, Padilla M, Kurosumi M, Matsumoto H, Inoue K, Horiguchi J, et al. HER2 intratumoral heterogeneity analyses by concurrent HER2 gene and protein assessment for the prognosis of HER2 negative invasive breast cancer patients. Breast Cancer Research and Treatment. 2016;158:99-111.
19. Lockhart AC, Liu Y, Dehdashti F, Laforest R, Picus J, Frye J, et al. Phase 1 Evaluation of [(64)Cu]DOTA-Patritumab to Assess Dosimetry, Apparent Receptor Occupancy, and Safety in Subjects with Advanced Solid Tumors. Molecular Imaging and Biology. 2016;18:446-53.
20. Wehrenberg-Klee E, Turker NS, Heidari P, Larimer B, Juric D, Baselga J, et al. Differential Receptor Tyrosine Kinase PET Imaging for Therapeutic Guidance. Journal of nuclear medicine : official publication, Society of Nuclear Medicine. 2016;57:1413-9.
21. Warnders FJ, Terwisscha van Scheltinga AG, Knuehl C, van Roy M, de Vries EF, Kosterink JG, et al. HER3 specific biodistribution and tumor uptake of 89Zr-MSB0010853 visualized by real-time and

non-invasive PET imaging. Journal of nuclear medicine : official publication, Society of Nuclear Medicine. 2017.
22. Bensch F, Lamberts LE, Srneenk MM, Jorritsma-Smit A, Lub-de Hooge MN, Van Scheltinga AGTT, et al. Zr-89-lumretuzumab PET imaging before and during HER3 antibody lumretuzumab treatment of solid tumor patients. J Clin Oncol. 2016;34.
23. van Dongen GA, Visser GW, Lub-de Hooge MN, de Vries EG, Perk LR. Immuno-PET: a navigator in monoclonal antibody development and applications. The oncologist. 2007;12:1379-89.
24. Da Pieve C, Allott L, Martins CD, Vardon A, Ciobota DM, Kramer-Marek G, et al. Efficient [18F]AlF Radiolabeling of ZHER3:8698 Affibody Molecule for Imaging of HER3 Positive Tumors. Bioconjugate Chemistry. 2016.
25. Rosestedt M, Andersson KG, Mitran B, Tolmachev V, Lofblom J, Orlova A, et al. Affibody-mediated PET imaging of HER3 expression in malignant tumours. Scientific reports. 2015;5:15226.
26. Pedersen K, Angelini PD, Laos S, Bach-Faig A, Cunningham MP, Ferrer-Ramon C, et al. A Naturally Occurring HER2 Carboxy-Terminal Fragment Promotes Mammary Tumor Growth and Metastasis. Mol Cell Biol. 2009;29:3319-31.
27. Eccles SA, Massey A, Raynaud FI, Sharp SY, Box G, Valenti M, et al. NVP-AUY922: a novel heat shock protein 90 inhibitor active against xenograft tumor growth, angiogenesis, and metastasis. Cancer Res. 2008;68:2850-60.
28. Girnita A, Girnita L, del Prete F, Bartolazzi A, Larsson O, Axelson M. Cyclolignans as inhibitors of the insulin-like growth factor-1 receptor and malignant cell growth. Cancer Res. 2004;64:236-42.
29. Workman P, Aboagye EO, Balkwill F, Balmain A, Bruder G, Chaplin DJ, et al. Guidelines for the welfare and use of animals in cancer research. Br J Cancer. 2010;102:1555–77.
30. Kramer-Marek G, Bernardo M, Kiesewetter DO, Bagci U, Kuban M, Aras O, et al. PET of HER2-positive pulmonary metastases with 18F-ZHER2:342 affibody in a murine model of breast cancer: comparison with 18F-FDG. Journal of Nuclear Medicine. 2012;53:939-46.
31. Kramer-Marek G, Kiesewetter DO, Capala J. Changes in HER2 Expression in Breast Cancer Xenografts After Therapy Can Be Quantified Using PET and (18)F-Labeled Affibody Molecules. Journal of Nuclear Medicine. 2009;50:1131-9.
32. Garcia-Carbonero R, Carnero A, Paz-Ares L. Inhibition of HSP90 molecular chaperones: moving into the clinic. Lancet Oncology. 2013;14:e358-69.
33. Altai M, Varasteh Z, Andersson K, Eek A, Boerman O, Orlova A. In vivo and in vitro studies on renal uptake of radiolabeled affibody molecules for imaging of HER2 expression in tumors. Cancer biotherapy & radiopharmaceuticals. 2013;28:187-95.
34. Deri MA, Zeglis BM, Francesconi LC, Lewis JS. PET imaging with (8)(9)Zr: from radiochemistry to the clinic. Nucl Med Biol. 2013;40:3-14.
35. Kumar V, Gu Y, Basu S, Berglund A, Eschrich SA, Schabath MB, et al. Radiomics: the process and the challenges. Magnetic Resonance Imaging. 2012;30:1234-48.
36. Parmar C, Grossmann P, Bussink J, Lambin P, Aerts HJ. Machine Learning methods for Quantitative Radiomic Biomarkers. Scientific reports. 2015;5:13087.
37. Chalkidou A, O'Doherty MJ, Marsden PK. False Discovery Rates in PET and CT Studies with Texture Features: A Systematic Review. PloS One. 2015;10:e0124165.
38. Slamon DJ, Leyland-Jones B, Shak S, Fuchs H, Paton V, Bajamonde A, et al. Use of chemotherapy plus a monoclonal antibody against HER2 for metastatic breast cancer that overexpresses HER2. New Engl J Med. 2001;344:783-92.
39. Piccart-Gebhart MJ, Procter M, Leyland-Jones B, Goldhirsch A, Untch M, Smith I, et al. Trastuzumab after adjuvant chemotherapy in HER2-positive breast cancer. New Engl J Med. 2005;353:1659-72.
40. Vogel CL, Cobleigh MA, Tripathy D, Gutheil JC, Harris LN, Fehrenbacher L, et al. Efficacy and safety of trastuzumab as a single agent in first-line treatment of HER2-overexpressing metastatic breast cancer. J Clin Oncol. 2002;20:719-26.
41. Sergina NV, Rausch M, Wang DH, Blair J, Hann B, Shokat KM, et al. Escape from HER-family tyrosine kinase inhibitor therapy by the kinase-inactive HER3. Nature. 2007;445:437-41.
42. Avril S, Muzic RF, Jr., Plecha D, Traughber BJ, Vinayak S, Avril N. (1)(8)F-FDG PET/CT for Monitoring of Treatment Response in Breast Cancer. Journal of Nuclear Medicine. 2016;57 Suppl 1:34S-9S.
43. Kramer-Marek G, Oyen WJ. Targeting the Human Epidermal Growth Factor Receptors with Immuno-PET: Imaging Biomarkers from Bench to Bedside. Journal of Nuclear Medicine. 2016;57:996-1001.

44. Terwisscha van Scheltinga AG, Lub-de Hooge MN, Abiraj K, Schroder CP, Pot L, Bossenmaier B, et al. ImmunoPET and biodistribution with human epidermal growth factor receptor 3 targeting antibody (8)(9)Zr-RG7116. mAbs. 2014;6:1051-8.
45. Orlova A, Malm M, Rosestedt M, Varasteh Z, Andersson K, Selvaraju RK, et al. Imaging of HER3-expressing xenografts in mice using a Tc-99m(CO)(3)-HEHEHE-Z(HER3:08699) affibody molecule. Eur J Nucl Med Mol I. 2014;41:1450-9.
46. Larimer BM, Phelan N, Wehrenberg-Klee E, Mahmood U. Phage Display Selection, In Vitro Characterization, and Correlative PET Imaging of a Novel HER3 Peptide. Molecular imaging and biology : MIB : the official publication of the Academy of Molecular Imaging. 2017.
47. Kong A, Rea D, Ahmed S, Beck JT, Lopez Lopez R, Biganzoli L, et al. Phase 1B/2 study of the HSP90 inhibitor AUY922 plus trastuzumab in metastatic HER2-positive breast cancer patients who have progressed on trastuzumab-based regimen. Oncotarget. 2016;7:37680-92.
48. Scaltriti M, Dawood S, Cortes J. Molecular pathways: targeting hsp90--who benefits and who does not. Clinical Cancer Research. 2012;18:4508-13.
49. Holland JP, Caldas-Lopes E, Divilov V, Longo VA, Taldone T, Zatorska D, et al. Measuring the Pharmacodynamic Effects of a Novel Hsp90 Inhibitor on HER2/neu Expression in Mice Using Zr-89-DFO-Trastuzumab. PloS One. 2010;5.
50. Oude Munnink TH, de Vries EG, Vedelaar SR, Timmer-Bosscha H, Schroder CP, Brouwers AH, et al. Lapatinib and 17AAG reduce 89Zr-trastuzumab-F(ab')2 uptake in SKBR3 tumor xenografts. Molecular pharmaceutics. 2012;9:2995-3002.
51. Whitesell L, Santagata S, Mendillo ML, Lin NU, Proia DA, Lindquist S. HSP90 empowers evolution of resistance to hormonal therapy in human breast cancer models. Proc Natl Acad Sci U S A. 2014;111:18297-302.
52. Cerami E, Gao J, Dogrusoz U, Gross BE, Sumer SO, Aksoy BA, et al. The cBio cancer genomics portal: an open platform for exploring multidimensional cancer genomics data. Cancer Discovery. 2012;2:401-4.

Legends to Figures

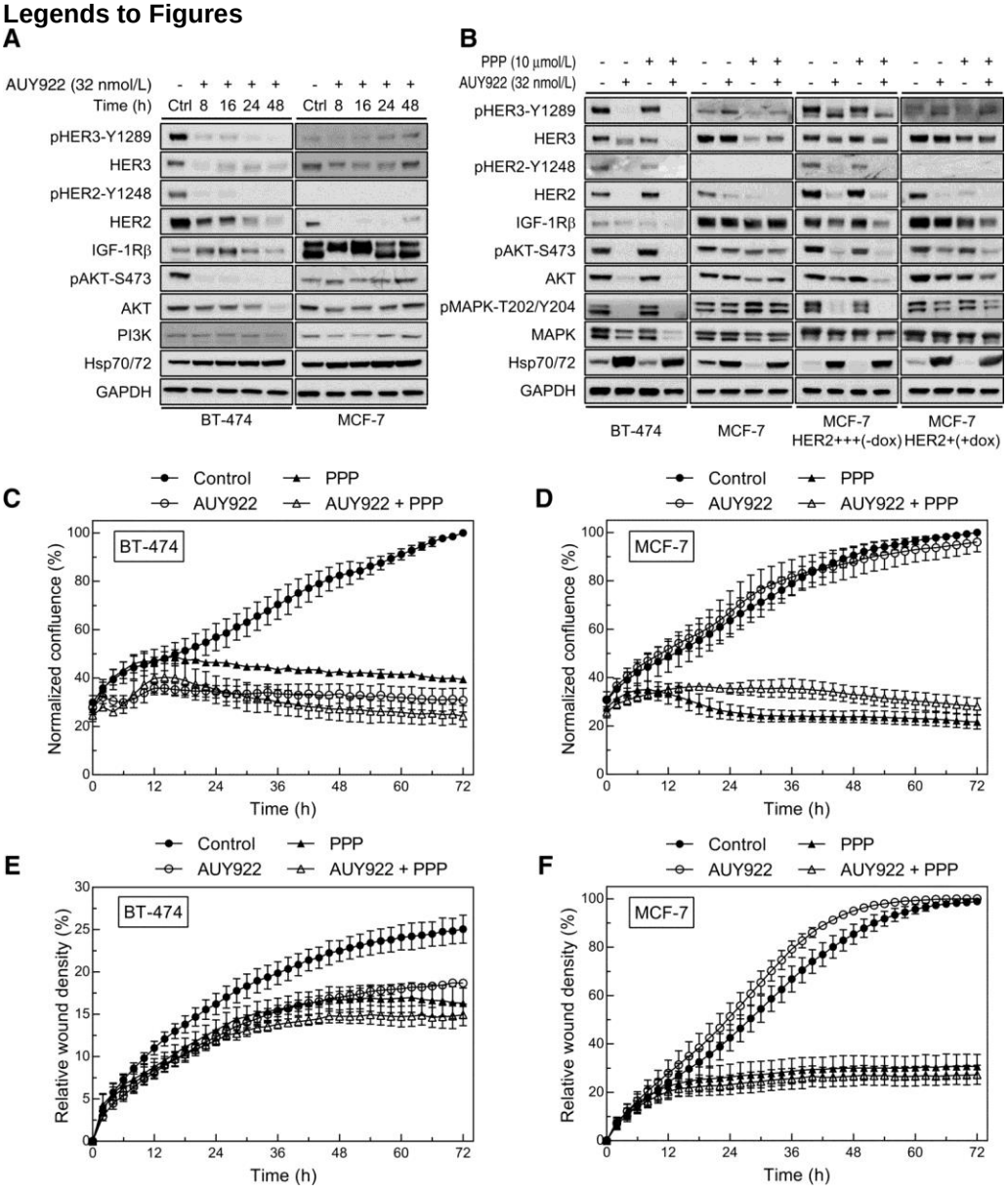

Fig. 1. AUY922 potentiates HER3-mediated downstream signaling and invasive phenotype in low-HER2 expressing cells. (A) Time course of AUY922 treatment (32 nM) in BT-474 and MCF-7 breast cancer cells up to 48 h. **(B)** BT-474, MCF-7, MCF-7-HER2 (-dox, induced HER2 expression), and MCF-7-HER2 (+dox, non-induced HER2 expression) cells were treated with AUY922 (32 nM) and/or PPP (10 mM) for 48 h. **(A** and **B)** HER receptors, IGF-1Rb, MAPK, and PI3K/AKT pathway activation were monitored by Western blot using whole cell lysates. Hsp70/72 expression was used as a surrogate for AUY922 treatment efficacy, and GAPDH as a loading control. **(C** and **D)** BT-474 and MCF-7 cells proliferation assessment for 72 h in response to AUY922 (32 nM) and/or PPP (10 mM). Confluence was monitored by phase contrast microscopy and expressed as the mean normalized confluence values ± SEM (*n* = 3 independent experiments) per time point. **(E** and **F)** Invasive phenotype monitoring of BT-474 and MCF-7 cells by scratch-wound assay, in response to AUY922 (32 nM) and/or PPP (10 mM) treatment for 72 h. Data are expressed as the mean relative wound density values ± SEM (*n* = 3 independent experiments) per time point.

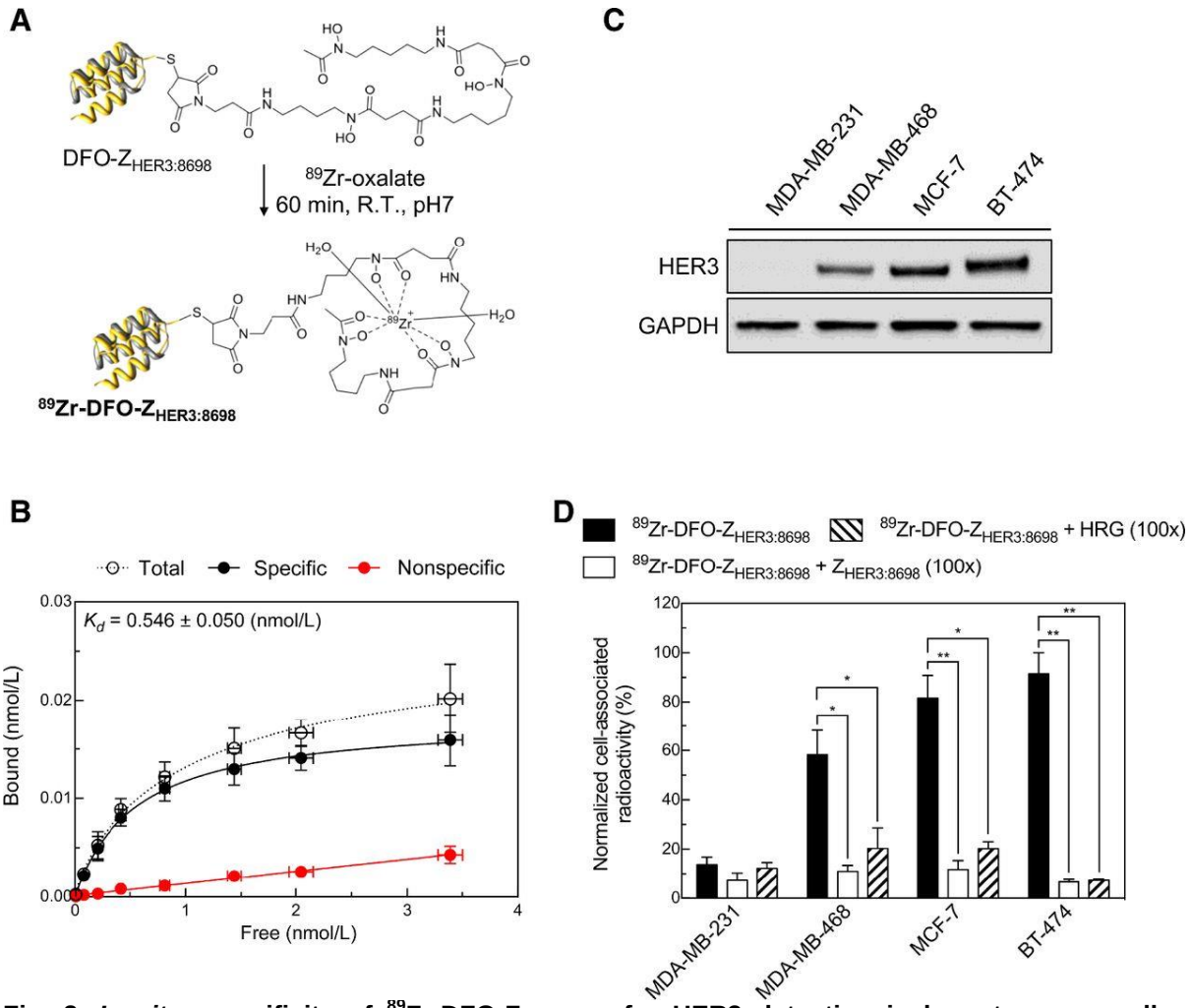

Fig. 2. *In vitro* specificity of ^{89}Zr-DFO-$Z_{HER3:8698}$ for HER3 detection in breast cancer cells. (A) Scheme illustrating the radiolabeling reaction of DFO-conjugated $Z_{HER3:8698}$ affibody molecule with the positron emitter ^{89}Zr. **(B)** Saturation binding of ^{89}Zr-DFO-$Z_{HER3:8698}$ to MCF-7 cells. The data are expressed as the mean values ± SEM (*n* = 3 independent experiments). **(C)** HER3 expression in a panel of breast cancer cell lines. Representative Western blot from whole cell lysates, with GAPDH used as the loading control. **(D)** *In vitro* binding specificity of ^{89}Zr-DFO-$Z_{HER3:8698}$ in breast cancer cells and specific blocking using 100-fold molar excess of either unlabeled $Z_{HER3:8698}$ or the natural HER3 ligand HRG. The data are expressed as the mean values ± SEM (*n* = 3 independent experiments). **P* = 0.0357; **P* = 0.0446; for MDA-MB468, ***P* = 0.0087; **P* = 0.015 for MCF-7, and ***P* = 0.009; ***P* = 0.0097 for BT-474 cells.

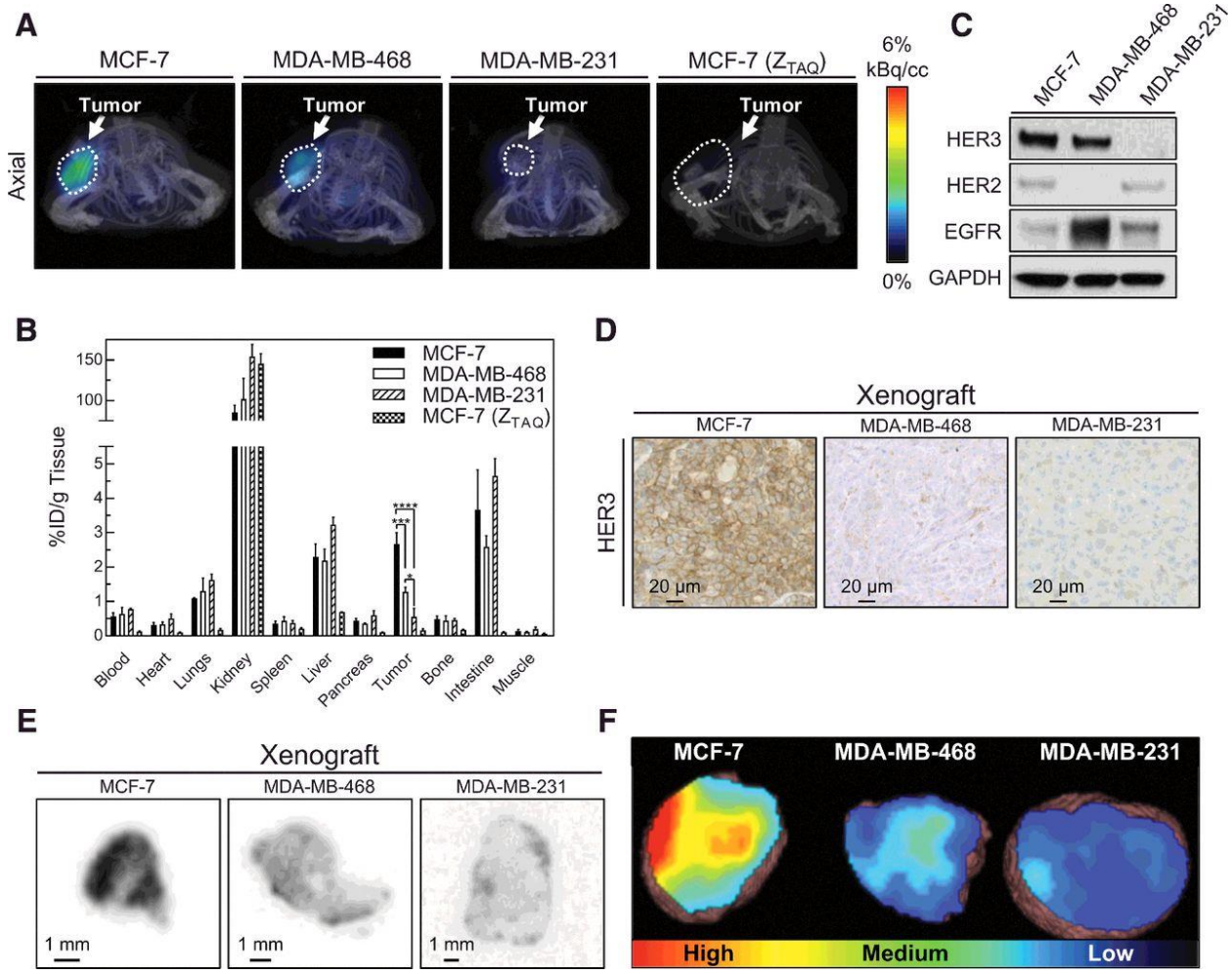

Fig. 3. PET/CT imaging and *ex vivo* analysis of ^{89}Zr-DFO-Z$_{HER3:8698}$ in mice bearing subcutaneous breast cancer xenografts. (A) Representative 15 min coronal fused PET/CT images of mice bearing MCF-7, MDA-MB-468, or MDA-MB-231 xenografts. The mice received ~ 8 MBq of either ^{89}Zr-DFO-Z$_{HER3:8698}$ or ^{89}Zr-DFO-Z$_{TAQ}$ via tail vein injection, with image acquisition taking place 3 h after injection. The arrowheads indicate the tumors and the kidneys. **(B)** *Ex vivo* biodistribution at 3 h after injection of the radioconjugates. Data are expressed as the mean values ± SD (n = 3 animals). *P = 0.0136; ***P = 0.0002; ****P < 0.0001. **(C)** Representative Western blot of whole tumor tissue lysates evaluating HER3, HER2 and EGFR expression in the indicated xenograft models. **(D)** Histopathological analysis of HER3 expression in MCF-7, MDA-MB-468, and MDA-MB-231 xenografts displaying the highest HER3 expression in MCF-7 xenografts and the lowest in MDA-MB-231. **(E)** Representative e*x vivo* autoradiography sections taken 3 h after injection of ^{89}Zr-DFO-Z$_{HER3:8698}$. **(F)** Autoradiography quantification from panel **E** as the intensity per region of interest area (A.U./cm^2). Data are expressed as the mean values ± SD (n = 10 sections). **P = 0.0028; ****P < 0.0001. **(G)** Representative segmented xenografts following PET/CT image acquisition 3 h after ^{89}Zr-DFO-Z$_{HER3:8698}$ injection. These images highlight the greater radioactivity accumulation observed in MCF-7 xenografts, and the heterogeneity of uptake across the tumor burden. Color map defined within the tumor volume only.

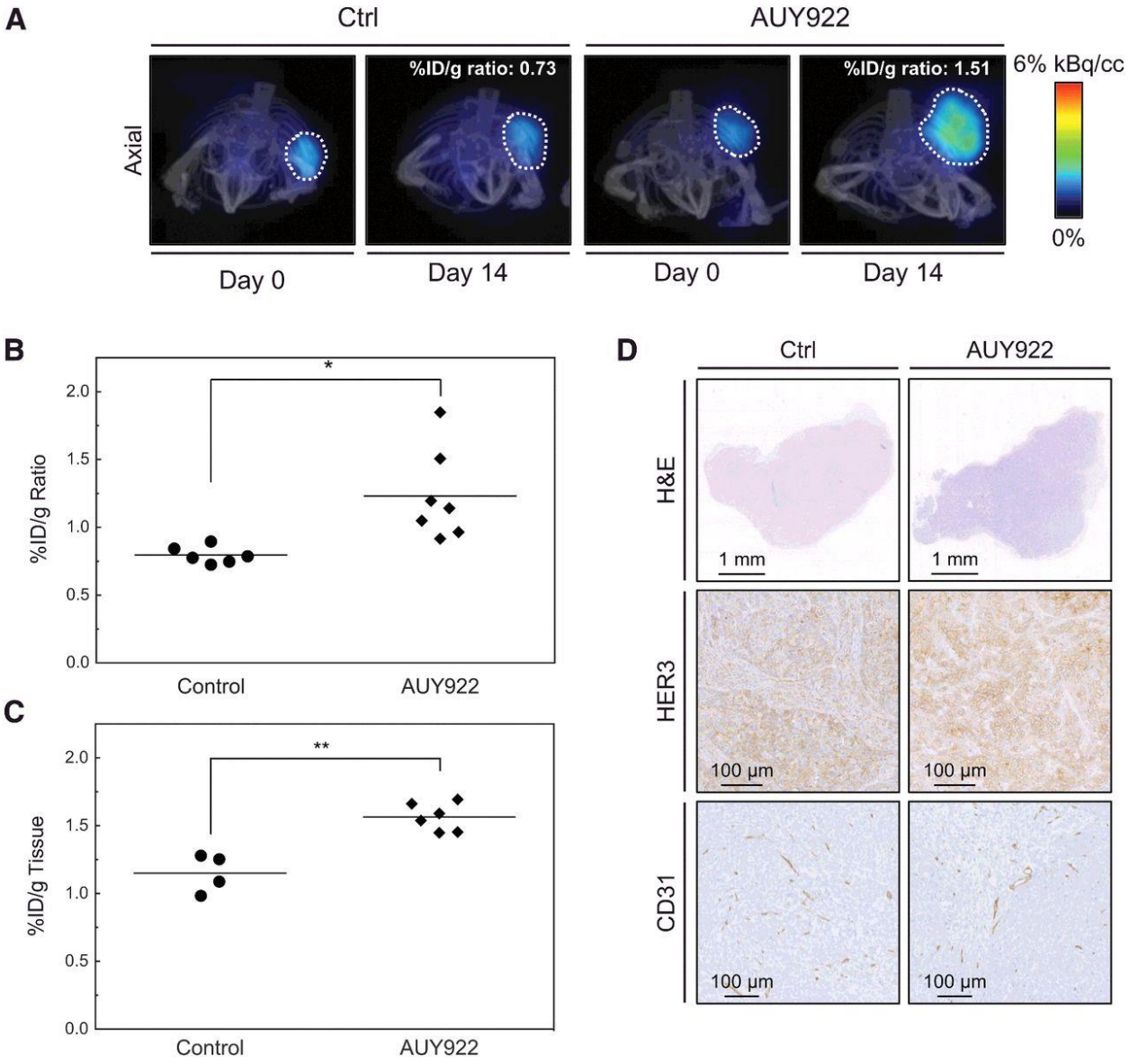

Fig. 4. AUY922 treatment response monitoring in MCF-7 xenografts by ^{89}Zr-DFO-$Z_{HER3:8698}$ PET/CT imaging. MCF-7 xenografts were randomized into two groups: control and treatment. The treatment group received 40 mg/kg of AUY922 i.p. every second day for a period of two weeks. **(A)** Representative axial fused PET/CT images of mice bearing MCF-7 tumors. Each mouse received 7.2-8.1 MBq of ^{89}Zr-DFO-$Z_{HER3:8698}$ via tail vein injection, with image acquisition taking place at 3 h after injection. The mice were imaged before initiating AUY922 treatment (day 0), and following administration of the last treatment dose (day 14). The %ID/g ratios were determined by dividing the %ID/g on day 14 by that obtained on day 0. **(B)** Scatter plot of the %ID/g ratios for both control (n = 6) and AUY922-treated mice (n = 7). The horizontal lines indicate the mean for each group. *P = 0.0131. **(C)** Scatter plot of the *ex vivo* tumor biodistribution at 3 h after injection of the radioconjugate on day 14, for both control (n = 4) and AUY922-treated mice (n = 6). The horizontal lines indicate the mean per group. **P = 0.0036. **(D)** Histopathological analysis of control and AUY922-treated MCF-7 xenografts. Tumor sections were stained with hematoxylin and eosin (H&E), HER3, or CD31.

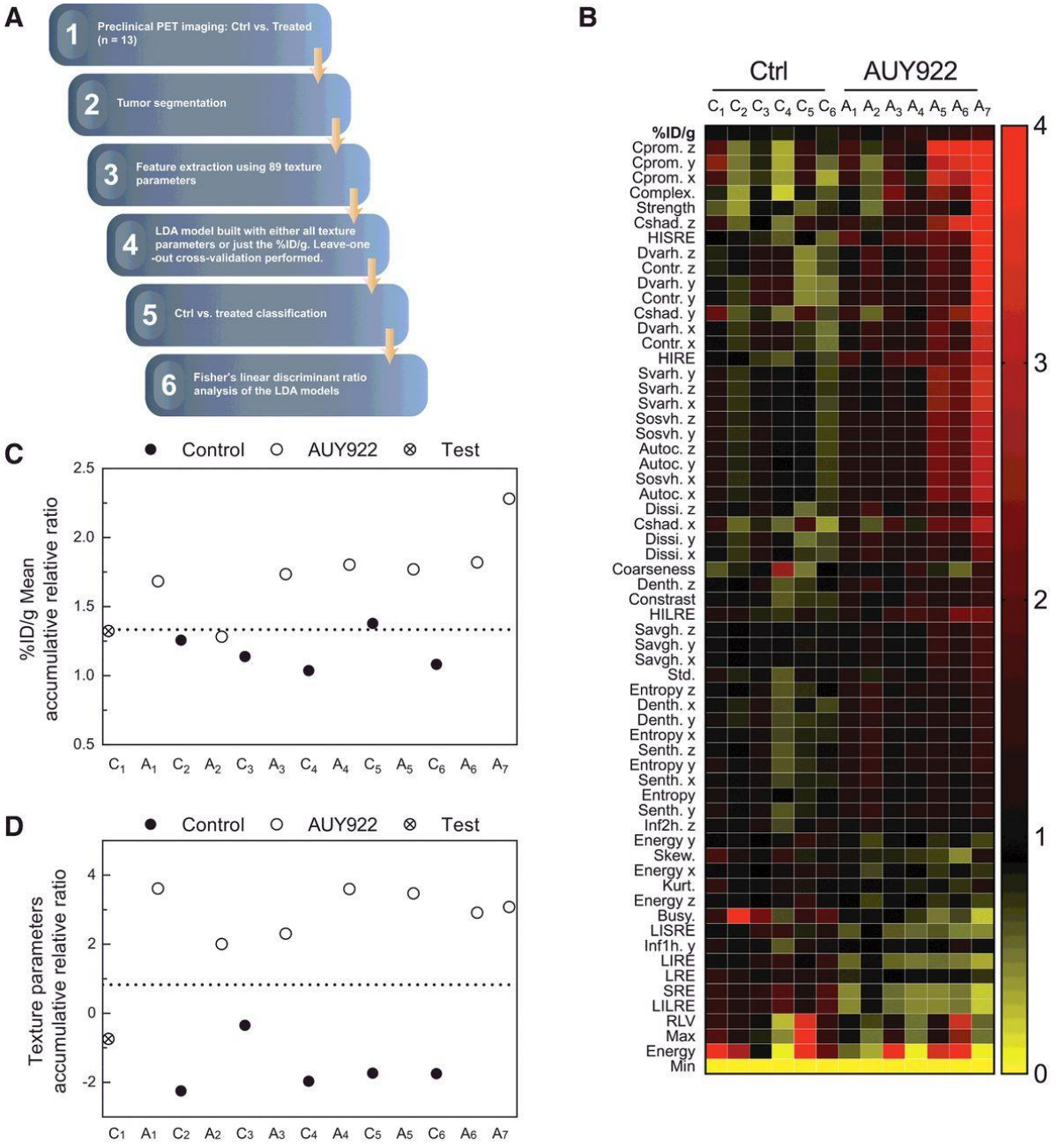

Fig. 5. ^{89}Zr-DFO-$Z_{HER3:8698}$ texture analysis identifies AUY922-treated MCF-7 xenografts. (A) Scheme illustrating the radiomic workflow from PET imaging data acquisition to LDA model testing. **(B)** Texture analysis heat map comprising the ratios of post/pre-treatment for extracted texture parameters per mouse (Control $C_{1\text{-}6}$, and AUY922 $A_{1\text{-}7}$). **(C)** Representative leave one out cross validation of the %ID/g LDA model, utilizing control mouse C_1 as the test subject. **(D)** Representative leave one out cross validation of the Texture LDA model, utilizing control mouse C_1 as the test subject. **(C** and **D)** The dashed lines represent a crude separation point between the two groups determined as the mean of the maximum and the minimum relative ratios of the control and AUY922 treatment group, respectively.

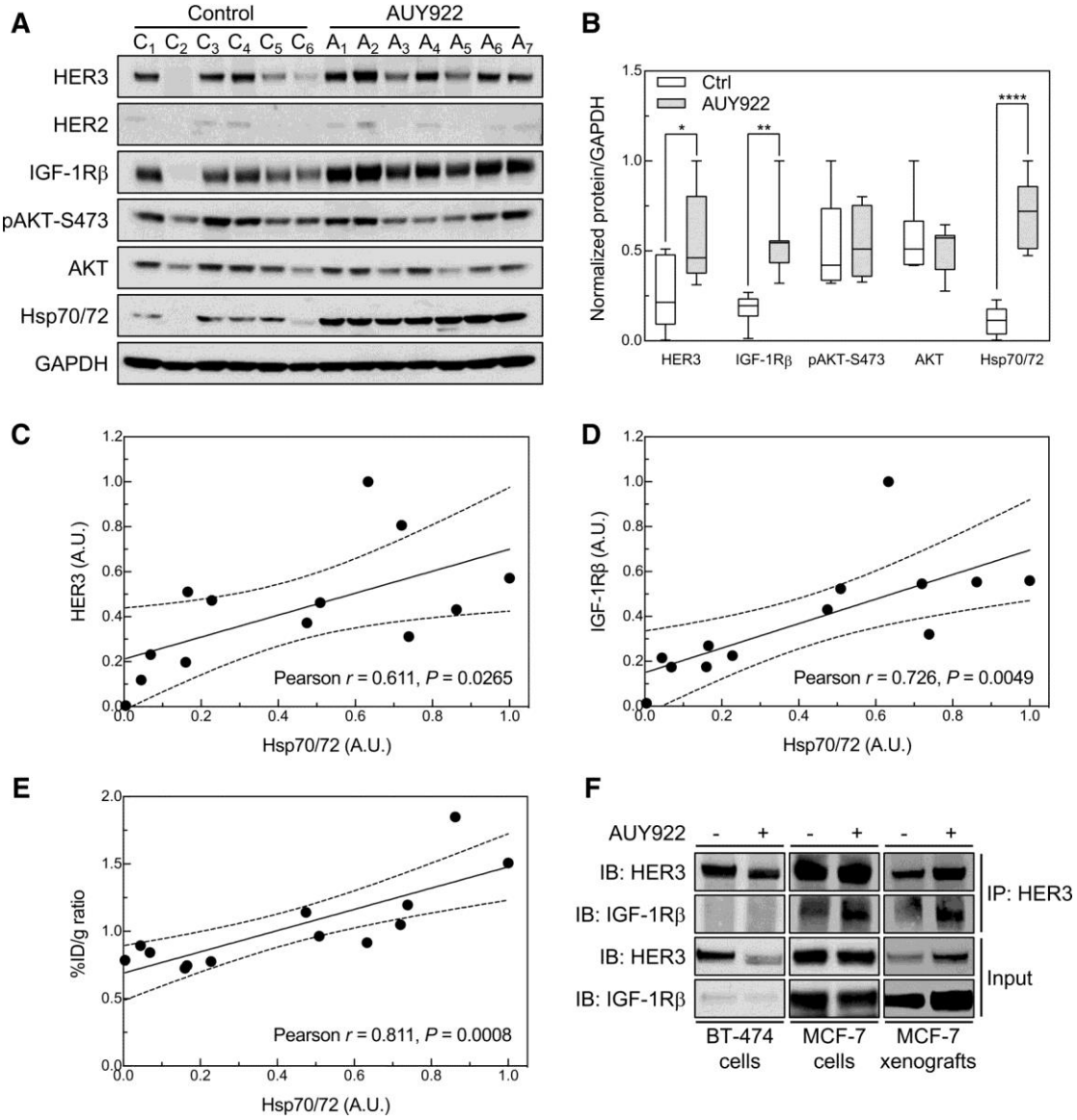

Fig. 6. AUY922 treatment promotes HER3-IGF-1Rβ mediated signalling in MCF-7 xenografts. (A) HER receptors, IGF-1Rβ, and PI3K/AKT pathway activation were monitored by Western blot using whole tissue lysates from all control and AUY922-treated mice. Hsp70/72 expression was used as a surrogate for AUY922 treatment efficacy, and GAPDH as a loading control. **(B)** Minimum to maximum box & whiskers plot of the quantified protein expression represented in A. Data are expressed as the normalized protein expression per antibody for control and AUY922 groups. The black lines represent the median value. **P* = 0.0306; ***P* = 0.0022; *****P* < 0.0001. **(C, D)** Correlation between HER3/IGF-1Rβ and Hsp70/72 protein expression per mouse. The dashed lines represent the ninety-five percent confidence levels. **(E)** Correlation between %ID/g ratios obtained from ^{89}Zr-DFO-$Z_{HER3:8698}$ PET images and Hsp70/72 protein expression per mouse. The dashed lines represent the ninety-five percent confidence levels. **(F)** BT-474 and MCF-7 cells were treated with 32 nM of AUY922 for 48 h. Equal amounts of whole cell lysates were immunoprecipitated with a mouse anti-HER3 antibody followed by Western blot analysis of HER3 and IGF-1Rβ. Whole tissue lysates from control mouse C_5 and AUY922-treated mouse A_6 were also immunoprecipitated against HER3 and analyzed by Western blot. Ten percent of the input lysates were used as loading controls.